



## High-sensitivity optical-fiber-compatible photodetector with an integrated CsPbBr<sub>3</sub>–graphene hybrid structure

JIN-HUI CHEN,<sup>1</sup> QIANG JING,<sup>1</sup> FEI XU,<sup>1,\*</sup> ZHEN-DA LU,<sup>1,2</sup> AND YAN-QING LU<sup>1,3</sup>

<sup>1</sup>National Laboratory of Solid State Microstructures, College of Engineering and Applied Sciences and Collaborative Innovation Center of Advanced Microstructures, Nanjing University, Nanjing 210093, China

<sup>2</sup>e-mail: luzhenda@nju.edu.cn

<sup>3</sup>e-mail: yqlu@nju.edu.cn

\*Corresponding author: feixu@nju.edu.cn

Received 3 April 2017; revised 9 June 2017; accepted 20 June 2017 (Doc. ID 291806); published 21 July 2017

**Assembling different materials into one optical fiber to realize multifunctional all-fiber devices is always a challenging task, mainly because the process is not compatible with current microfabrication technology. Although various devices have been proposed to achieve “all-fiber” optoelectronic functions, most of these devices cannot connect seamlessly with the mainstream optical fiber system (silica): this is a serious impairment to their further implementation in practical applications. Here, we present an integration approach that directly combines low-dimensional optoelectronic materials (CsPbBr<sub>3</sub> nanocrystals and graphene) onto the facet of a standard silica fiber to construct a high-performance photodetector, which can detect light with a power as low as 10<sup>-11</sup> W with photoresponsivity as high as 2 × 10<sup>4</sup> A/W. Moreover, it has an extraordinary light–matter interaction path beneficial to enhancing light absorption and realizing self-passivation and protection. Because of its compatibility with current established optical fiber systems, this technique could provide a highly versatile, reproducible, and low-cost method to integrate novel zero-, one-, and two-dimensional materials and deliver more sophisticated functionalities.** © 2017 Optical Society of America

**OCIS codes:** (060.2340) Fiber optics components; (040.5160) Photodetectors; (060.2380) Fiber optics sources and detectors; (130.0250) Optoelectronics.

<https://doi.org/10.1364/OPTICA.4.000835>

Integrating distinct conductors, semiconductors, and insulators into an optical fiber platform to achieve in-line multifunctional devices for photonic, optoelectronic, acoustic, and even biochemical applications has recently attracted much attention [1–4]. Among them, the all-fiber photodetector (FPD) shows eye-catching features for its capabilities in distributed photodetection [5]. More important, since the photodetector is an indispensable device in current optical communication systems, an FPD

can realize both photon transport and detection in a single optical fiber. However, most of the multifunctional fibers are not perfectly compatible with current mature optical fiber (silica) systems because of their different geometries and structures [1,2]. Photoresponsivity is another factor that limits the range of practical applications of the FPDs reported in literature [5,6], typically being far less than that of the commercial photodetectors.

In recent years, organic–inorganic hybrid perovskites have been considered to be very attractive photovoltaic materials for their superior optoelectronic properties and low-cost fabrication technology [7,8]. Engineering the interface and optimizing the architecture, the power conversion efficiency of hybrid perovskites based solar cells leaped from 4% to over 20% [8]. Apart from the photovoltaic applications, hybrid perovskites also show great promise in light emitting diodes [9,10], laser [11,12], and photodetectors [13–15]. The research of hybrid perovskites also triggers the recent development of all-inorganic perovskite nanocrystals (IPNCs). The IPNCs show high photoluminescence quantum yield, tunable bandgap depending on their sizes and composition, and relatively good stability in an ambient environment [16,17]. All of these are indications that IPNCs have great potential in optoelectronic applications [18–21]. Moreover, the solution-processed technology endows them with the capability to fit into many platforms, including both flexible and corrugated substrates.

Here we demonstrate a novel device: an ultrasensitive, highly fiber-compatible photodetector (FCPD) fabricated by integrating solution-processed CsPbBr<sub>3</sub> nanocrystals (NCs) and multilayered graphene into the facet of a single silica fiber (Fig. 1). By using CsPbBr<sub>3</sub> NCs as a highly efficient light absorption layer and graphene as an ultrafast photocarriers transporting layer [22,23], our FCPD can detect light powers as low as 10<sup>-11</sup> W with a photoresponsivity as high as 2 × 10<sup>4</sup> A/W, which is, to our knowledge, a record value among the other reported optical fiber photodetectors [5,6]. In contrast to multimaterials fiber [1], our platform can seamlessly connect with the current optical fiber system and can accommodate versatile optoelectronic materials [7,16,18,24,25]. We believe our results may provide a new path to designing all-in-

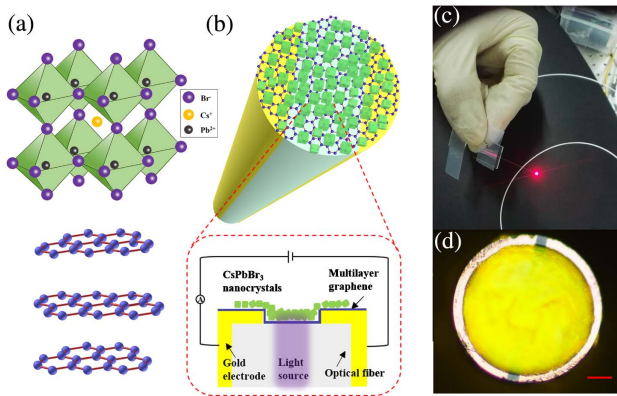


**Fig. 1.** Design of the FCPD device. (a) Schematic of the cubic perovskite  $\text{CsPbBr}_3$  NCs and multilayered graphene crystal structures. (b) Device configuration of an FCPD with  $\text{CsPbBr}_3$  NCs and graphene composite structure. The two separated Au electrodes (yellow sections) are deposited at the facet of an optical fiber and its lateral walls. The inset is the cross-sectional view of the FCPD. (c) Photograph of a fabricated FCPD transporting a red light source. The strong scattering effect at the end face of the optical fiber is caused by the  $\text{CsPbBr}_3$  NCs films. (d) Optical microscope image of an FCPD. The bright yellow film is the self-assembled  $\text{CsPbBr}_3$  NCs films, which serves as a photoconductor layer. The scale bar is 20  $\mu\text{m}$ .

fiber multifunctional devices and enable many practical applications in optical communications and sensing.

**Optical fiber integrating photodetector design.** The crystal structures of  $\text{CsPbBr}_3$  NCs and multilayered graphene are illustrated in Fig. 1(a). The high-quality NCs were synthesized by a modified hot-injecting method (see Supplement 1) [16]. The schematic structure of the FCPD is shown in Fig. 1(b). A cleaved optical fiber (SMF-28, Corning) was fabricated with a pair of gold electrodes and sequentially deposited multilayered graphene and  $\text{CsPbBr}_3$  NCs (see Supplement 1). We adopt a dip-coating method [26,27] to directly transfer a layer of multilayered graphene onto the facet of a fiber without any polymer, like poly(methyl methacrylate) (PMMA). Interestingly, the self-assembled circular  $\text{CsPbBr}_3$  film on fiber is obtained using a simple isopropanol treating process (see Supplement 1). The intrinsic absorption coefficient for  $\text{CsPbBr}_3$  NCs is  $0.8 \times 10^5 \text{ cm}^{-1}$  for 400 nm light wavelength [28], which means that NCs film with a thickness of 500 nm is sufficient to absorb light power according to the law of Bouguer–Lambert–Beer. Different from other reported graphene–perovskite hybrid photodetectors [22,23,29], in which the light source irradiates from the perovskites sides, in our case, the light illuminates the graphene layer first and then the NCs layers. As a result, the control on the thickness of the  $\text{CsPbBr}_3$  NCs film is less strict, disregarding the photocarriers recombination effect and electron conductivity issue for a thick  $\text{CsPbBr}_3$  film. The film thickness on the fiber can reach several micrometers [Fig. 1(d), see Supplement 1], in contrast to sub-micrometer thickness perovskites in a chip-based photodetector [22,23,29]. The relatively thick  $\text{CsPbBr}_3$  film is beneficial for light absorption and may also serve as a self-passivated layer for the inner active matter, which improves the stability of the FCPD. Figure 1(c) shows a photograph of an as-fabricated FCPD injected with a red light source. The strong scattering effect on the fiber is attributed to the aggregated NCs on the fiber end face (see Supplement 1).

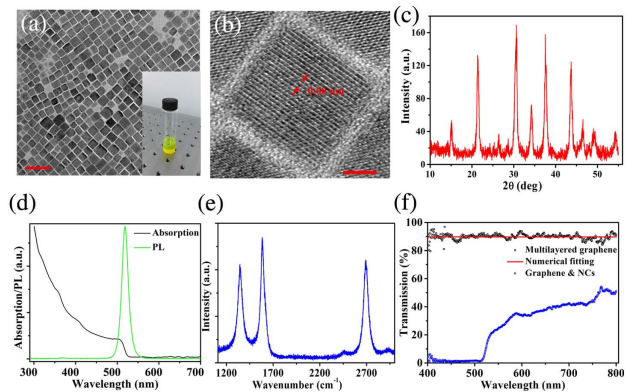


**Fig. 2.** Properties of  $\text{CsPbBr}_3$  NCs and graphene. (a) TEM image of  $\text{CsPbBr}_3$  NCs. The scale bar represents 50 nm. The inset is the photograph of the  $\text{CsPbBr}_3$  NCs dispersed in cyclohexane. (b) Typical high-resolution TEM image of a  $\text{CsPbBr}_3$  NC. The scale bar is 5 nm. (c) X-ray diffraction patterns of  $\text{CsPbBr}_3$  NCs. (d) Absorption and PL spectra of  $\text{CsPbBr}_3$  NCs, which show the direct bandgap characteristic of  $\text{CsPbBr}_3$ . (e) Raman spectrum of multilayered graphene. (f) Transmittance spectrum of a multilayered graphene and composite graphene- $\text{CsPbBr}_3$  structure, both of which are deposited on the facet of an optical fiber.

**Nanomaterials and device characterization.** A TEM image in Fig. 2(a) shows the morphology and uniformity of as-synthesized  $\text{CsPbBr}_3$  NCs. The NCs have a square or rectangular shape with a measured edge distribution maximum peak of around 14 nm. We can find that the NCs have a narrow size distribution. A typical high-resolution TEM image of a single NC is shown in Fig. 2(b). The atomic columns are clearly resolved, and the measured lattice parameter of 0.6 nm is in good agreement with the results from the powder x-ray diffraction (XRD) pattern in Fig. 2(c), showing the cubic phase of  $\text{CsPbBr}_3$ . And the inset of Fig. 2(a) is the camera image of  $\text{CsPbBr}_3$  NCs dispersed in cyclohexane. Figure 2(d) demonstrates the UV-visible absorption spectrum and photoluminescence spectrum (PL) of  $\text{CsPbBr}_3$ . The full width at half-maximum (FWHM) of the PL peak is  $\sim 18$  nm, located at a wavelength of  $\sim 518.8$  nm, which agrees well with the absorption edge of NCs. The quantum yield of  $\text{CsPbBr}_3$  NCs we used is as high as 78%, which is comparable with reported results [16]. The Raman fingerprint of multilayered graphene is shown in Fig. 2(e). The substrate of the graphene for Raman characterization is  $\text{SiO}_2/\text{Si}$  for measuring convenience. By measuring the transmittance spectrum of graphene, shown in Fig. 2(f), and fitting numerically (see Supplement 1), we find that the number of graphene layers is  $\sim 6$ . The transmittance spectrum of an FCPD is also measured in Fig. 2(f). We can find that nearly all the light power with a wavelength under 520 nm is absorbed thanks to the thick  $\text{CsPbBr}_3$  film structure. The non-unit transmittance for light wavelength over 550 nm might be attributed to the strong scattering effect of  $\text{CsPbBr}_3$  film [Fig. 1(c), see Supplement 1] and absorption in the multilayered graphene.

**Photoresponse characterizations of the FCPD device.** Figure 3(a) shows the optical and electrical circuit for measuring the photoresponse of the FCPD. Since the FCPD naturally integrates with an optical fiber system, the light power is transported in the optical fiber waveguide and used to illuminate the FCPD. The generated electrical signal is collected and analyzed by a

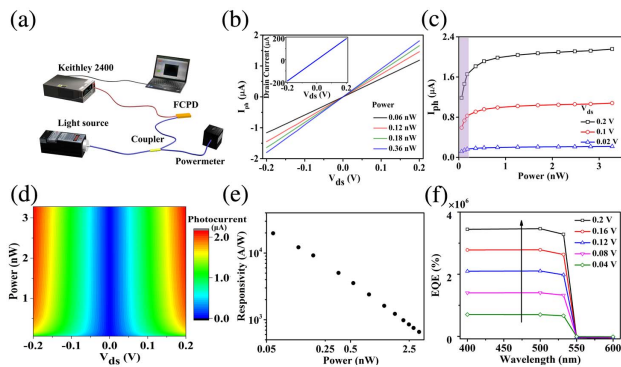


**Fig. 3.** Device performance of the FCPD. (a) Photoelectrical characterization system for our FCPD. (b) Dependence of generated photocurrent on incident light power (at 400 nm) and applied bias voltage. The inset shows the linear I-V curve of the FCPD in darkness. (c) Photocurrent of the FCPD for different light power and applied voltage. The marked violet region is the quasi-linear light power response for the FCPD. (d) Mapping photocurrent ( $|I_{ph}|$ ) spectra relate to the incident light power and applied voltage. (e) Typical responsivity of our FCPD to illuminating light power at a wavelength of 400 nm and bias of 0.2 V. (f) EQE of our FCPD as a function of spectral wavelength at different bias voltage. The light power is set as  $\sim 0.2$  nW.

sourceter. To calibrate the input power on the FCPD, we employed a double arms configuration (referential arm and experimental arm). The linear I-V curve of the FCPD in darkness, as illustrated in the inset of Fig. 3(b), indicates the ohmic contact between electrodes and photoconductor layers. The dependence of photocurrents ( $I_{ph} = I_{light} - I_{dark}$ ) on applied voltage and light power (at 400 nm) is plotted in Fig. 3(b). The photocurrent relationship to light power is shown in Fig. 3(c) for three different bias voltages. It can be found that the saturated light power for the FCPD is as low as 1 nW, and the quasi-linear power response can be less than 0.2 nW. Considering the limited effective area of the FCPD ( $\sim 80 \mu\text{m}^2$ ), the power density is as large as  $1.25 \text{ mW/cm}^2$  for even 1 nW input light power, which is far higher than usually selected light density for device characterizations [22,23,30]. The light power range measure in this study is only limited by the available referential powermeter in our lab (0.1 nW resolution, S150C, Thorlabs). The absolute photocurrent values ( $|I_{ph}|$ ) mapping correlated to light power and applied voltage is summarized in Fig. 3(d). We can see that the photocurrent generation is almost symmetric to bias voltage, which is the expected behavior of the ohmic contact of the FCPD.

The responsivity ( $R = I_{ph}/P_{light}$ ) is an important figure of merit of a photodetector. Figure 3(e) shows the light power dependent responsivity curves under 400 nm illumination at 0.2 V voltage. The highest responsivity of the FCPD is  $\sim 2 \times 10^4$  A/W for 0.06 nW light illumination. The external quantum efficiency (EQE) is calculated from the definition  $\text{EQE} = Rhc/e\lambda$ , where  $h$  is the Planck constant,  $c$  is the light velocity in vacuum,  $e$  is the electron charge, and  $\lambda$  is the light wavelength. So, the calculated highest EQE should be as large as  $\sim 6 \times 10^6\%$ . As far as we know, this is the highest value ever reported for an all-fiber photodetector [5,6]. It is known that the responsivity for a photodetector is highly dependent on the power intensity. In our case, the minimum power intensity is as large as  $75 \mu\text{W/cm}^2$ , which is still far larger than the typical power density measured in other studies

[22,31]. Much higher responsivity is expected when the illuminated power intensity is further reduced (see Supplement 1 for the comparison of the performances between our FCPD and other photodetectors). Moreover, if a higher voltage is applied on the FCPD, the responsivity can be further improved. This is because the higher voltage can reduce the carrier transition time in the photoconducting channel. And the gain factor of the device is higher, thus higher responsivity. However, the dark current is compromised consequently. To characterize the wavelength-dependent photogain of our FCPD, the EQE versus wavelength at different voltage with the light power fixed at 0.2 nW is shown in Fig. 3(f). The EQE value in the UV-visible band shows a short-pass characteristic, which is consistent with the absorption spectrum of CsPbBr<sub>3</sub> NCs. We also calculate the noise equivalent power (NEP) and the detectivity ( $D^*$ ) of our device. When the input power is 0.06 nW, the NEP and  $D^*$  are  $3.9 \times 10^{-16} \text{ WHz}^{-1/2}$  and  $8.6 \times 10^{10}$  Jones, respectively, which is comparable to commercial silicon photodiodes [32] and is mainly limited by the large dark current of graphene.

The ultrahigh responsivity (gain) of our FCPD can be attributed to the photogating effect, which has been investigated before [22,23,29]. It has been found that when perovskite NCs contact with graphene, the latter can be electron doped by perovskites in order to balance the Fermi level. The built-in electric field formed at the interface can block the photon-generated electron, while driving the holes diffusing to the graphene layers. The remaining electrons in the perovskites can exert negative gate voltages and induce a net photocurrent through capacitive coupling. Thanks to the long lifetime of photocarriers in perovskites and the ultrafast carrier mobility in graphene, the photogain can be greatly enhanced. Considering the intrinsic carrier mobility and the discontinuity of the formed film, the carrier mobility is low for CsPbBr<sub>3</sub>-only film. And it can be expected that the responsivity for CsPbBr<sub>3</sub> is small. As for graphene, the carrier lifetime is very short, although the carrier mobility is high. And the responsivity is also very small. As a result, the combination of CsPbBr<sub>3</sub> and graphene contributes to the high responsivity of our device. We measured the I-V curves for the graphene-only device and the graphene-NCs hybrid device (see Supplement 1). It can be found that after depositing a layer of NCs, the conductivity of the device is changed, which indirectly indicates the charge migrating effect between graphene and NCs. We have also conducted a contrast experiment by fabricating graphene-only and CsPbBr<sub>3</sub> NCs-only FCPD with similar structure. The graphene-only FCPD shows very weak and unstable photoresponse while the CsPbBr<sub>3</sub> NCs show weak photoresponse ( $\sim 0.06$  A/W) with fast response speed (see Supplement 1).

**Stability measurement of the FCPD device.** The temporal response of the FCPD was measured using a 400 nm diode laser with light power fixed at 0.1 nW. The laser is mechanically chopped, and the generated photocurrent is modulated consequently, as shown in Fig. 4(a). We evaluated the FCPD photoresponse by periodically switching on and off illumination light at three different voltages, namely 0.05 V, 0.1 V, and 0.2 V bias voltage. The dynamical change of the photocurrent is nearly the same for different applied voltages. However, the response speed of our FCPD is very slow, with rise and fall time calculated to be 3.1 s and 24.2 s, respectively, by using the stretched exponential function [29,33]. The long rise and fall time of the FCPD might be attributed to the residual long-chain organic ligands on

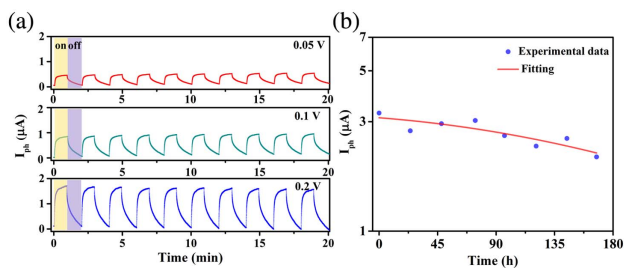


**Fig. 4.** Transient response and long-term stability of the FCPD. (a) Temporal response of the FCPD at different applied voltages with the input light source fixed at  $\sim 0.1$  nW (at 400 nm). (b) Photocurrent of the FCPD measured in air at room temperature over one week with illuminating light power fixed at  $\sim 0.1$  nW (at 400 nm). The applied voltage is 0.2 V.

CsPbBr<sub>3</sub> surface, which block the photocarrier transport between particles. Moreover, the considerably thick CsPbBr<sub>3</sub> film (in the micrometers scale) may also prolong the transport time for photocarriers. The response time can be improved by increasing the isopropanol washing times or using short-chain organic ligands. The long-term stability of perovskites materials is a common concern for researchers [7,17]. For organic-inorganic hybrid perovskites, it is commonly accepted that moisture and heat lead to device degradation. As for the all-inorganic perovskites, the two factors will be much relieved because of their structural stability. Although there are many works on the organic-inorganic mixed or all-inorganic perovskites-based photodetectors, only a few of these show their long-term stability evaluation [30]. To characterize the stability of our FCPD, the illuminating light power is set as  $\sim 0.1$  nW ( $0.125$  mW/cm<sup>2</sup>) using a 400 nm light source. The measurement is conducted over a week, and the result is demonstrated in Fig. 4(b). Numerical fitting shows that the  $1/e$  decay time of our FCPD is 320 h. It should be noted that the entire experiment is conducted completely in an ambient environment without any encapsulation. The mechanism of gradual degradation for our FCPD is not very clear and might be attributed to the photo-degradation effect of CsPbBr<sub>3</sub> NCs [34]. Further research is needed to investigate the stability of all-inorganic perovskites materials.

In summary, we report an all-in fiber photodetector fabricated by integrating CsPbBr<sub>3</sub> NCs and multilayered graphene onto the end face of an optical fiber. This kind of photodetector is highly compatible with the current optical fiber system with ultrahigh photoresponsivity ( $2 \times 10^4$  A/W). Our platform is straightforward and can be readily transferred to other optoelectronic materials, including zero-dimensional, one-dimensional, and two-dimensional materials. This novel design method may provide a new route to the realization of all-fiber multifunctional devices.

**Funding.** National Natural Science Foundation of China (NSFC) (61475069, 61535005); National Science and Technology Major Projects (2017YFA0303700).

**Acknowledgment.** The authors thank Prof. Xue-jin Zhang for the help with the experiments.

See Supplement 1 for supporting content.

## REFERENCES

1. A. Abouraddy, M. Bayindir, G. Benoit, S. Hart, K. Kuriki, N. Orf, O. Shapira, F. Sorin, B. Temelkuran, and Y. Fink, *Nat. Mater.* **6**, 336 (2007).
2. A. Canales, X. Jia, U. P. Froriep, R. A. Koppes, C. M. Tringides, J. Selvidge, C. Lu, C. Hou, L. Wei, and Y. Fink, *Nat. Biotechnol.* **33**, 277 (2015).
3. S. Egusa, Z. Wang, N. Chocat, Z. M. Ruff, A. M. Stolyarov, D. Shemuly, F. Sorin, P. T. Rakich, J. D. Joannopoulos, and Y. Fink, *Nat. Mater.* **9**, 643 (2010).
4. M. Fokine, L. E. Nilsson, Å. Claesson, D. Berlemont, L. Kjellberg, L. Krummenacher, and W. Margulis, *Opt. Lett.* **27**, 1643 (2002).
5. M. Bayindir, F. Sorin, A. F. Abouraddy, J. Viens, S. D. Hart, J. D. Joannopoulos, and Y. Fink, *Nature* **431**, 826 (2004).
6. X. Sun, C. Qiu, J. Wu, H. Zhou, T. Pan, J. Mao, X. Yin, R. Liu, W. Gao, and Z. Fang, *Opt. Express* **23**, 25209 (2015).
7. Y. Zhao and K. Zhu, *Chem. Soc. Rev.* **45**, 655 (2015).
8. S. D. Stranks and H. J. Snaith, *Nat. Nanotechnol.* **10**, 391 (2015).
9. Z. K. Tan, R. S. Moghaddam, M. L. Lai, P. Docampo, R. Higler, F. Deschler, M. Price, A. Sadhanala, L. M. Pazos, and D. Credgington, *Nat. Nanotechnol.* **9**, 687 (2014).
10. N. Wang, L. Cheng, R. Ge, S. Zhang, Y. Miao, W. Zou, C. Yi, Y. Sun, Y. Cao, and R. Yang, *Nat. Photonics* **10**, 699 (2016).
11. F. Deschler, M. Price, S. Pathak, L. E. Klintberg, D. D. Jarausch, R. Higler, S. Hüttner, T. Leijtens, S. D. Stranks, and H. J. Snaith, *J. Phys. Chem. Lett.* **5**, 1421 (2014).
12. Q. Zhang, S. T. Ha, X. Liu, T. C. Sum, and Q. Xiong, *Nano Lett.* **14**, 5995 (2014).
13. L. Dou, Y. M. Yang, J. You, Z. Hong, W. H. Chang, G. Li, and Y. Yang, *Nat. Commun.* **5**, 5404 (2014).
14. Y. Fang, Q. Dong, Y. Shao, Y. Yuan, and J. Huang, *Nat. Photonics* **9**, 679 (2015).
15. Y. Guo, C. Liu, H. Tanaka, and E. Nakamura, *J. Phys. Chem. Lett.* **6**, 535 (2015).
16. L. Protesescu, S. Yakunin, M. I. Bodnarchuk, F. Krieg, R. Caputo, C. H. Hendon, R. X. Yang, A. Walsh, and M. V. Kovalenko, *Nano Lett.* **15**, 3692 (2015).
17. J. Liang, C. Wang, Y. Wang, Z. Xu, Z. Lu, Y. Ma, H. Zhu, Y. Hu, C. Xiao, and X. Yi, *J. Am. Chem. Soc.* **138**, 15829 (2016).
18. Y. Wang, X. Li, J. Song, L. Xiao, H. Zeng, and H. Sun, *Adv. Mater.* **27**, 7101 (2015).
19. A. Swarnkar, R. Chulliyil, V. K. Ravi, M. Irfanullah, A. Chowdhury, and A. Nag, *Angew. Chem., Int. Ed. Engl.* **54**, 15424 (2015).
20. P. Ramasamy, D. H. Lim, B. Kim, S. H. Lee, M. S. Lee, and J. S. Lee, *Chem. Commun.* **52**, 2067 (2015).
21. S. Yakunin, L. Protesescu, F. Krieg, M. I. Bodnarchuk, G. Nedelcu, M. Humer, L. G. De, M. Fiebig, W. Heiss, and M. V. Kovalenko, *Nat. Commun.* **6**, 8056 (2015).
22. D. H. Kwak, D. H. Lim, H. S. Ra, P. Ramasamy, and J. S. Lee, *RSC Adv.* **6**, 65252 (2016).
23. Y. Wang, Y. Zhang, Y. Lu, W. Xu, H. Mu, C. Chen, H. Qiao, J. Song, S. Li, and B. Sun, *Adv. Opt. Mater.* **3**, 1389 (2015).
24. S. Das, J. A. Robinson, M. Dubey, H. Terrones, and M. Terrones, *Annu. Rev. Mater. Res.* **45**, 1 (2014).
25. S. Z. Butler, S. M. Hollen, L. Cao, Y. Cui, J. A. Gupta, H. R. Gutiérrez, T. F. Heinz, S. S. Hong, J. Huang, and A. F. Ismach, *ACS Nano* **7**, 2898 (2013).
26. J. Ma, W. Jin, H. L. Ho, and J. Y. Dai, *Opt. Lett.* **37**, 2493 (2012).
27. B. C. Zheng, S. C. Yan, J. H. Chen, G. X. Cui, F. Xu, and Y. Q. Lu, *Laser Photonics Rev.* **9**, 517 (2015).
28. R. J. De, M. Ibáñez, P. Geiregat, G. Nedelcu, W. Walravens, J. Maes, J. C. Martins, D. I. Van, M. V. Kovalenko, and Z. Hens, *ACS Nano* **10**, 2071 (2016).
29. Y. Lee, J. Kwon, E. Hwang, C. H. Ra, W. J. Yoo, J. H. Ahn, J. H. Park, and J. H. Cho, *Adv. Mater.* **27**, 41 (2015).
30. R. Dong, Y. Fang, J. Chae, J. Dai, Z. Xiao, Q. Dong, Y. Yuan, A. Centrone, X. C. Zeng, and J. Huang, *Adv. Mater.* **27**, 1967 (2015).
31. C. Xie and F. Yan, *ACS Appl. Mater. Interfaces* **9**, 1569 (2017).
32. M. Buscema, J. O. Island, D. J. Groenendijk, S. I. Blanter, G. A. Steele, V. D. Z. Hs, and A. Castellanosgomez, *Chem. Soc. Rev.* **44**, 3691 (2015).
33. M. Martens, J. Schlegel, P. Vogt, and F. Brunner, *Appl. Phys. Lett.* **98**, 211114 (2011).
34. J. Chen, D. Liu, M. J. Al-Marri, L. Nuutila, H. Lehtivuori, and K. Zheng, *Sci. China Mater.* **59**, 719 (2016).